

# Methods for Evaluating the Temperature Structure-Function Parameter Using Unmanned Aerial Systems and Large-Eddy Simulation

Charlotte E. Wainwright · Timothy A. Bonin ·  
Phillip B. Chilson · Jeremy A. Gibbs ·  
Evgeni Fedorovich · Robert D. Palmer

Received: 4 August 2014 / Accepted: 29 December 2014 / Published online: 9 January 2015  
© Springer Science+Business Media Dordrecht 2015

**Abstract** Small-scale turbulent fluctuations of temperature are known to affect the propagation of both electromagnetic and acoustic waves. Within the inertial-subrange scale, where the turbulence is locally homogeneous and isotropic, these temperature perturbations can be described, in a statistical sense, using the structure-function parameter for temperature,  $C_T^2$ . Here we investigate different methods of evaluating  $C_T^2$ , using data from a numerical large-eddy simulation together with atmospheric observations collected by an unmanned aerial system and a sodar. An example case using data from a late afternoon unmanned aerial system flight on April 24 2013 and corresponding large-eddy simulation data is presented and discussed.

**Keywords** Large-eddy simulation · Sodar · Structure-function parameter · Unmanned aerial system

## 1 Introduction

Temperature fluctuations associated with atmospheric turbulence can strongly affect the propagation of electromagnetic and acoustic waves in the atmosphere (Tatarskii 1961). Understanding the impact of these fluctuations on wave propagation and scattering is important for the correct interpretation of returns from remote-sensing instruments such as radars and sodars. An improved understanding of the spatial variability of temperature allows for better interpretation of sodar and radar returns, and thus maximizes the extractable information from these returns.

---

C. E. Wainwright (✉) · P. B. Chilson · R. D. Palmer  
Advanced Radar Research Center and School of Meteorology,  
University of Oklahoma, Norman, OK, USA  
e-mail: charlotte.wainwright@ou.edu

T. A. Bonin · J. A. Gibbs · E. Fedorovich  
School of Meteorology, University of Oklahoma, Norman, OK, USA

A useful parameter for quantifying the spatial variability of temperature in the atmosphere is the structure function for temperature,  $(\delta T)^2$ , which is calculated as

$$\overline{(\delta T)^2}(\mathbf{r}, t) = \overline{[T(\mathbf{x}, t) - T(\mathbf{x} + \mathbf{r}, t)]^2}, \quad (1)$$

where the overbar represents ensemble averaging,  $T$  is temperature,  $\mathbf{x}$  is a position vector,  $\mathbf{r}$  is a separation vector, and  $t$  is time. If the separation distance  $r = |\mathbf{r}|$  is within the inertial subrange of turbulence scales, where the temperature fluctuations are locally isotropic, then the temperature structure function can be represented as

$$\overline{(\delta T)^2} = C_T^2 r^{2/3}, \quad (2)$$

where  $C_T^2$  is the structure-function (or structure) parameter for temperature (Tatarskii 1971). Knowledge of the temperature structure-function parameter is important not only for better interpretation of instrument returns, but also because the refractive index structure-function parameter,  $C_n^2$ , is related to  $C_T^2$  in monostatic configurations via

$$C_n^2 \propto C_1 C_T^2 + C_2 C_{Tq} + C_3 C_q^2, \quad (3)$$

where  $C_{Tq}$  is the temperature-humidity structure-function parameter and  $C_q^2$  is the structure-function parameter for humidity, and  $C_1$ ,  $C_2$ , and  $C_3$  are constants whose value vary for acoustic and electromagnetic scattering (following Tatarskii 1961, 1971; Wyngaard et al. 1971).

Knowledge of the vertical profiles of  $C_n^2$  is important for a wide range of topics, including optics and ground-to-satellite communications (e.g., Tunick 2005). Fluctuations in optical wave-propagation parameters are of importance for astroclimatic studies, as these fluctuations depend upon  $C_n^2$ . Hence  $C_n^2$  fields are used to determine optimal sites for astronomical observatories (e.g., Gur'yanov et al. 1992; Travouillon et al. 2003; Petenko et al. 2014a).

Experimental methods for evaluating  $C_T^2$  have typically involved ground-based temperature measurements (e.g., Kunkel et al. 1981), thermometers mounted on tethered balloons or radiosondes (e.g., Readings and Butler 1972; Balsley 2008), or airborne measurements (e.g., Thomson et al. 1978). These in situ methods require either two sets of simultaneously recorded temperature measurements separated by a known distance, or high-temporal resolution measurements of temperature, wind speed and direction, plus invoking Taylor's frozen field turbulence hypothesis (Taylor 1938).

Remote sensing instruments can also be used to derive  $C_T^2$ . Acoustic remote sensing has previously been used to evaluate  $C_T^2$  through use of the sodar returned power (Neff 1975). Many previous studies have compared  $C_T^2$  derived from sodars to those directly evaluated by methods mentioned in the previous paragraph, finding fair agreement (e.g., Asimakopoulos et al. 1976; Weill et al. 1980; Gur'yanov et al. 1987; Kumar et al. 2011). A comprehensive analysis of the statistical characteristics of variations in sodar-derived  $C_T^2$  under convective conditions can be found in Petenko et al. (2014b).

Scintillometry can also be used to derive  $C_T^2$  values (e.g., Frehlich 1992), since the refraction of light in the atmosphere is primarily controlled by temperature fluctuations. Scintillometers provide path-averaged  $C_T^2$  values that typically represent spatial scales of temperature fluctuations from tens of metres to a few kilometres. Previous studies have shown that scintillometer-derived  $C_T^2$  values compare well with those estimated from sonic-anemometer temperature and wind measurements (e.g., Wood et al. 2013).

More recently, unmanned aerial systems (UASs) have become a widely-employed technique for meteorological studies (e.g., Holland et al. 2001; Shuqing et al. 2004; Spiess et al.

2007; van den Kroonenberg et al. 2008). Since UAS platforms can provide high-resolution temperature, wind, and location data, they are well placed to examine  $C_T^2$ . This capability has recently been explored by van den Kroonenberg et al. (2012), who used a UAS to study  $C_T^2$  over a heterogeneous land surface on two summer days.  $C_T^2$  values were derived from temperature data recorded during straight-line and square-path flights, and then compared to  $C_T^2$  derived from sonic-anemometer measurements. Good agreement was found in the diurnal variation in  $C_T^2$  measured by the sonic thermoanemometers and UAS.

Aside from using measurements from in situ or remote sensing instruments,  $C_T^2$  has also been examined through numerical simulation. The advancement of the large-eddy simulation (LES) technique has provided a tool to examine structure-function parameters of atmospheric flow in four dimensions both from LES data (Peltier and Wyngaard 1995; Cheinet and Cumin 2011; Wilson and Fedorovich 2012; Maronga et al. 2013), and through the development of the LES-based numerical radar simulators (Muschinski et al. 1999; Scipión et al. 2008). One advantage of using LES data for this purpose is that both the spatial and temporal variability of  $C_T^2$  can be examined across a range of scales and also in relation to the separation-distance dependence. In addition, the use of LES allows for the testing of different methods to derive  $C_T^2$  from the same data, something that cannot be easily achieved in the field.

The present work examines how UAS can be employed to evaluate the structure-function parameter for temperature, and proposes a UAS simulator capable of ingesting LES data. This allows for a comparison of theoretical UAS  $C_T^2$  retrievals with those from the LES generated using different retrieval algorithms. Our study also compares  $C_T^2$  measurements derived from a UAS and a sodar operated at the University of Oklahoma's Kessler Atmospheric and Ecological Field Station (KAEFS). The KAEFS facility is a heavily instrumented field site located in rural Oklahoma, encompassing a mixture of rolling grassland and heterogeneous vegetation. A LES experiment was conducted with the domain centered upon the field site and the time period encompassing that during which the UAS and sodar were operational. The LES data, in the form of highly temporally- and spatially-resolved flow fields, is used to test the UAS simulator, and also to directly evaluate  $C_T^2$ . This allows for a sensible comparison of several methods of deriving  $C_T^2$  and an examination of the effects of spatial and temporal averaging on the derived values.

The rest of the paper is organized as follows: in Sect. 2, the UAS platform used for the experiment is described. Details on the UAS simulator are presented in Sect. 3. Section 4 explains the methods used to extract  $C_T^2$  from the LES data, from the UAS simulator and real UAS data, and from the sodar. A description of the experiment conducted using LES data in conjunction with UAS, and results from the experiment are presented in Sect. 5. Conclusions are provided in Sect. 6.

## 2 Unmanned Aerial System

The University of Oklahoma operates an unmanned aerial system known as the Small Multifunction Autonomous Research and Teaching Sonde (SMARTSonde, Bonin et al. 2012, 2013). The SMARTSonde is primarily used to investigate the structure of the atmospheric boundary layer. The particular airframe employed in this study was a Funjet Ultra, which has a wingspan of 0.8 m and a weight of approximately 1 kg, an endurance of 30 min, and a cruising speed of  $15 \text{ m s}^{-1}$ . The SMARTSonde is equipped with sensors to measure atmospheric temperature, pressure, and relative humidity; the response time for the pressure sensor is 0.5 s, accurate to  $\pm 1.5 \text{ Pa}$ . The response time and measurement accuracy for the relative humidity sensor are 8 s and  $\pm 1.8 \%$ , respectively, while the accuracy of the temperature sensor

measurement is  $\pm 0.3$  K. The time constant of the sensor was calculated through calibration, resulting in a time constant of 3 s for an airspeed of  $15 \text{ m s}^{-1}$ .

The SMARTSonde employs the open source Paparazzi autopilot system for autonomous flight, although a pilot with a radio controller manually operates the aircraft during take-off and landing. A more complete description of the UAS package can be found in [Bonin et al. \(2013\)](#). As an update, an inertial measurement unit has recently been integrated into the autopilot for determination of the aircraft altitude.

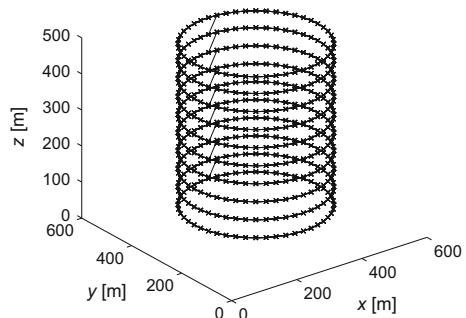
### 3 UAS Simulator

A UAS simulator was developed in order to examine the relative merits of different methods of retrieving  $C_T^2$  from UAS measurements. The simulator ingests three-dimensional fields of temperature from large-eddy simulation (LES) output, which are sampled in a manner that mimics the flight plan of the UAS in the atmosphere.

Many aspects of the UAS simulator are defined by the user, in the way that the simulator can be used to emulate desired flight plans. The SMARTSonde utilizes two main flight patterns (plans) for boundary-layer research: the first is a steady helical ascent, which is used alongside specially designed retrieval algorithms to derive the wind speed and direction ([Bonin et al. 2013](#)). The second flight pattern is applied to examine the spatial structure and statistical properties of thermodynamic quantities such as temperature and humidity. This flight plan entails the SMARTSonde flying in a number of consecutive circles at each height of interest before ascending to the next height (as illustrated in [Fig. 1](#)). The UAS simulator can mimic both of these flight plans, but it is the second plan ([Fig. 1](#)) that is used in the current study.

User-defined flight-plan characteristics in the UAS simulator include the circle radius, the desired airspeed, the height interval at which to sample, and the amount of time for the simulated UAS to remain at each height before ascending. These flight characteristics are then translated into Cartesian coordinates within the LES domain at times corresponding to each measurement (based upon the desired flight speed). The LES temperature and wind data are spatially and temporally interpolated to provide temperature and horizontal wind component ( $u$  in the  $x$  direction and  $v$  in the  $y$  direction) measurements at each sampling point. Fields of  $u$  and  $v$  are required to enable advection correction, which is discussed in [Sect. 4.2](#). The structure-function parameter for temperature is evaluated using these virtual temperature and wind measurements, using the method described in [Sect. 4.2](#).

**Fig. 1** The flight path used by the UAS for measuring temperature, which can be used to calculate  $C_T^2$



## 4 Methods for Evaluating $C_T^2$

Four methods of evaluating  $C_T^2$  are utilized herein: direct evaluation from LES output; evaluation using a simulated UAS flight within the LES domain; derivation from UAS data recorded during a field experiment; and derivation from sodar return power. Thorough descriptions of each of these methods are provided in the following subsections.

### 4.1 Evaluating $C_T^2$ from LES Data

In evaluating  $C_T^2$  from LES data, only the four-dimensional (three spatial coordinates and time) temperature field is required, along with knowledge of the grid spacing and time resolution of the generated field. The method calculates a running sum of squared temperature difference values for a given separation distance in a specific direction and within a horizontal cross-section of the domain located at a particular height. Once squared differences from the entire horizontal plane have been summed, an average is calculated. This procedure is repeated for each height and time before proceeding to the next separation distance. This method is explained in detail in [Wilson and Fedorovich \(2012\)](#) for the refractive index  $n$ .

The squared temperature differences  $(\delta T)^2$  are calculated in four separate directions:  $x$  (zonal differences),  $y$  (meridional differences), the positive diagonal (henceforth referred to as  $xy$ ), and the negative diagonal (henceforth  $yx$ ). These calculations are performed as

$$(\delta T)^2|_x(x, x_i, y, z, t) = [T(x, y, z, t) - T(x - x_i, y, z, t)]^2, \quad (4)$$

$$(\delta T)^2|_y(x, y, y_i, z, t) = [T(x, y, z, t) - T(x, y - y_i, z, t)]^2, \quad (5)$$

$$(\delta T)^2|_{xy}(x, x_i, y, y_i, z, t) = [T(x, y, z, t) - T(x - x_i, y - y_i, z, t)]^2, \quad (6)$$

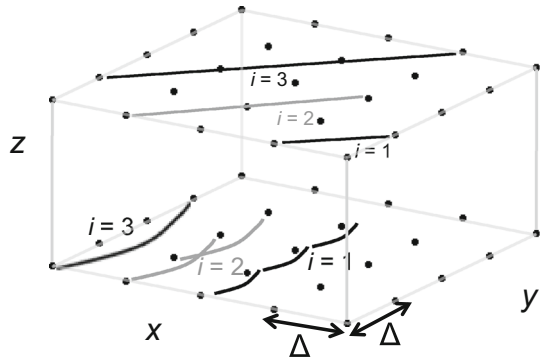
and

$$(\delta T)^2|_{yx}(x, x_i, y, y_i, z, t) = [T(x, y, z, t) - T(x - x_i, y + y_i, z, t)]^2. \quad (7)$$

In Eqs. 3–6,  $x_i$  is the separation distance in the  $x$ -direction and  $y_i$  is the separation distance in the  $y$ -direction. Note that in Eqs. 5 and 6,  $x_i = y_i$ , such that the squared temperature differences are calculated on strict diagonals only. All the separation distances used to calculate  $(\delta T)^2|_x$  and  $(\delta T)^2|_y$  are multiples of the LES horizontal grid spacing,  $\Delta = \Delta x = \Delta y$ , so no interpolation between numerical grid points in the horizontal plane is needed. The separation distances used to calculate  $(\delta T)^2|_{xy}$  and  $(\delta T)^2|_{yx}$  are multiples of the minimal diagonal distance ( $\Delta xy = \sqrt{\Delta x^2 + \Delta y^2}$ ).

The method outlined above is illustrated in Fig. 2. The upper plane illustrates the calculation of  $(\delta T)^2|_{xy}$  (Eq. 5) for separation distances of  $x_i = y_i = \Delta, 2\Delta$  and  $3\Delta$ , and the lower plane shows the calculation of  $(\delta T)^2|_y$  for separation distances of  $y_i = \Delta, 2\Delta$  and  $3\Delta$ . This method is applied in Sect. 5 to the LES data described in Sect. 5.1, and the results are described in Sect. 5.2. The LES model used to test the method has a grid spacing of 5 m. The  $(\delta T)^2|_x$  values are calculated for each separation distance  $x_i = i\Delta$  where  $i = 1, 2, \dots, 50$ , and for each height and time of interest. The maximum value of  $i$  was set to 50 to give a maximum separation distance  $r$  of 250 m, which is a typical diameter of the UAS flight circles. The calculated  $(\delta T)^2|_x$  values are then spatially averaged for each separation distance  $i\Delta$ . This method is repeated for Eq. 4 using separation distances  $y_i = i\Delta$  where  $i = 1, 2, \dots, 50$  as before, and for Eqs. 5 and 6 using  $x_i = y_i = i\Delta$  where  $i = 1, 2, \dots, 50$  (equating to straight-line separation distances of  $i\Delta xy = \sqrt{2 \times 1^2}, \sqrt{2 \times 2^2}, \dots, \sqrt{2 \times 50^2}$ ). The corresponding structure-function counterparts to the squared differences in Eqs. 3–6 are calculated as

**Fig. 2** Illustration of the methods of evaluating  $C_T^2$  directly from the LES. The lower  $z$  level illustrates the  $(\delta T)^2|_y$  method and the upper  $z$  level shows the  $(\delta T)^2|_{xy}$  method



$$\overline{(\delta T)^2}|_x(z, i \Delta) = \langle (\delta T)^2|_x(x, x_i, y, z, t) \rangle_{x,y,t}, \tag{8}$$

$$\overline{(\delta T)^2}|_y(z, i \Delta) = \langle (\delta T)^2|_y(x, y, y_i, z, t) \rangle_{x,y,t}, \tag{9}$$

$$\overline{(\delta T)^2}|_{xy}(z, i \Delta xy) = \langle (\delta T)^2|_{xy}(x, x_i, y, y_i, z, t) \rangle_{x,y,t}, \tag{10}$$

and

$$\overline{(\delta T)^2}|_{yx}(z, i \Delta xy) = \langle (\delta T)^2|_{yx}(x, x_i, y, y_i, z, t) \rangle_{x,y,t}, \tag{11}$$

where the angled brackets denote the averaging within each horizontal plane and in time.

Conceptually, the notion of  $C_T^2$  makes sense only when the turbulence is assumed to be isotropic and homogeneous within the inertial subrange of spatial scales. Use of LES allows for examination of the validity of the isotropy assumption by comparing the  $\overline{(\delta T)^2}$  values for different directions. If the turbulence is close to the isotropic state within certain scale ranges, there should be only minor differences between the values of  $\overline{(\delta T)^2}$  values calculated using Eqs. 7–10 for the corresponding ranges of the separation distances.

#### 4.2 Evaluating $C_T^2$ from the UAS Simulator

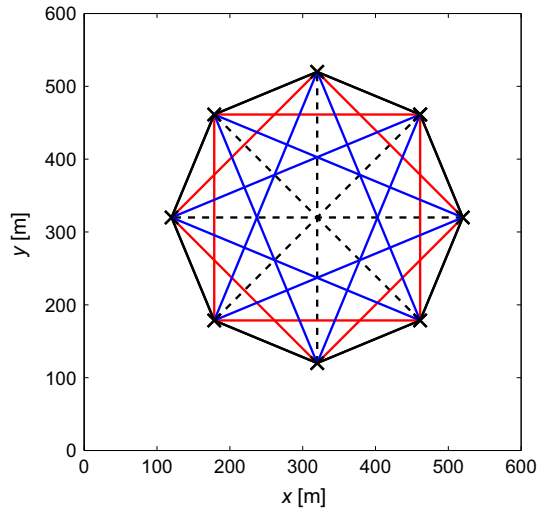
The UAS simulator provides  $T$ ,  $u$ , and  $v$  values corresponding to the simulated location of the UAS within the LES domain for the duration of the simulated flight. For each individual measurement height, the temperature data are combined to include all possible data pairs (providing  $n(n - 1)/2$  unique pairs of temperature data, where  $n$  is the total number of temperature measurements recorded at that height). A squared temperature difference,  $(\delta T)^2$ , can then be calculated from each temperature pair.

As the simulated UAS coordinates are known at every time, the separation distance between the two data points,  $r$ , is then calculated for each temperature pair. The calculation of the temperature difference pairs and separation distance is illustrated in Fig. 3. The separation distances are modified to account for the advection of turbulence past the UAS by the wind, as detailed in Bonin et al. (2015). With advection correction, the separation distance is calculated as

$$r = \sqrt{(x_i - u \Delta t)^2 + (y_i - v \Delta t)^2}, \tag{12}$$

where  $x_i$  and  $y_i$  are the separation distances in the zonal and meridional directions,  $u$  and  $v$  are the instantaneous zonal and meridional wind speeds in  $\text{m s}^{-1}$ , and  $\Delta t$  is the time between consecutive measurements. Advection correction is not performed when  $C_T^2$  is evaluated directly from the LES as described in Sect. 4.1, since in this case all the temperature values at a given height correspond to the same moment of time. However, the real and simulated

**Fig. 3** Illustration of the methods of evaluating  $C_T^2$  from the UAS flight and simulated flight. Only eight data points around the circle are used for clarity. In this example,  $C_T^2$  is calculated at four separation distances, 153 m (*solid black line*), 283 m (*red line*), 370 m (*blue line*), and 400 m (*dashed black line*). The radius of the circular flight path is 200 m



UAS both experience advection of turbulence past the UAS by the wind. To account for the advection of turbulence on time scales equal to the time between measurements, Taylor’s frozen turbulence hypothesis is utilized.

The temperature pairs are separated into bins based on  $r^{2/3}$ , and the structure function,  $(\delta T)^2$ , is calculated by averaging all the  $(\delta T)^2$  values within each bin. The structure-function parameter for temperature,  $C_T^2$ , is then evaluated for each bin using Eq. 2.

### 4.3 Evaluating $C_T^2$ from UAS Data

The method used for evaluating  $(\delta T^2)$ , and subsequently  $C_T^2$ , from data recorded by the UAS is very similar to that described in the previous sub-section for the UAS simulator. The spatial coordinates of the UAS during the flight are recorded by a global positioning system (GPS) sensor at the same temporal rate that the temperature is recorded. The wind components  $u$  and  $v$  can be estimated using the heading direction, throttle, and instantaneous airspeed data recorded by the UAS. The method used to estimate  $C_T^2$  from the UAS data is outlined in detail in Bonin et al. (2015).

The recorded temperature data are divided into height batches based upon the height recorded by the GPS. This is done manually to ensure that time periods during take-off, final descent, landing, and during which the plane is ascending from one height to the next, are excluded. The recorded locations, temperatures, and derived wind components are then used to calculate  $(\delta T^2)$  and  $C_T^2$  values as outlined in Sect. 4.2.

### 4.4 Evaluating $C_T^2$ from Sodar Data

The method of retrieving  $C_T^2$  from sodar data makes use of the returned sodar power (as described in, e.g., Weill et al. 1980),

$$P_R = P_T G A_e \sigma_s \frac{c\tau \exp(-2\alpha h)}{2 h^2}, \tag{13}$$

where  $P_T$  is transmitted power,  $G$  is the gain of the antenna,  $A_e$  is the antenna effective area in  $m^2$ ,  $\sigma_s$  is the acoustic backscattering coefficient at  $180^\circ$  in  $m^{-1}$ ,  $c$  is the speed of

sound in  $\text{m s}^{-1}$ ,  $\tau$  is the acoustic pulse duration in s,  $h$  is the range of the signal in m, and  $\alpha$  represents acoustic attenuation due to atmospheric absorption. It should be noted that many commercially available sodars scale the returned power and then present the data in units of dB with an arbitrary zero. This is done to minimize the storage space required for the data, since unscaled values of  $P_R$  are typically on the order of  $10^{-16}$  W. The effective backscattering cross-section per unit of scattering volume per unit of solid angle,  $\sigma_s$ , is related to  $C_T^2$  as

$$\sigma_s = 4 \times 10^{-3} \lambda^{-1/3} \frac{C_T^2}{T^2}, \quad (14)$$

where  $\lambda$  is the sodar wavelength in m, and  $T$  is in K (following Little 1969). The sodar provides, as output data, values of  $P_R$  and  $h$ , whilst  $P_T$ ,  $G$ ,  $A_e$ , and  $\tau$  are functions of the sodar system used. The value of  $\lambda$  is indirectly set by the sodar user, and is a function of the acoustic transmit frequency,  $f$ , and the speed of sound,  $c$ , calculated as  $\lambda = c/f$ .

The acoustic attenuation  $\alpha$  is calculated according to ISO9613-1 (1993). The relation for  $\alpha$  is not reproduced here for brevity. The full calculation of  $\alpha$  requires input of vertical profiles of temperature  $T$  and specific humidity  $q$  encompassing the range over which  $\alpha$  is to be calculated, and the acoustic transmit frequency  $f$ . Since the sodar does not measure relative humidity, additional instrumentation is needed to provide these data. In our case, the UAS can provide the necessary temperature and humidity data. In order to evaluate  $\alpha$ , the  $T$  and  $q$  values obtained from the UAS are interpolated to the sodar measurement heights. This naturally restricts the calculation of  $\alpha$ , and thus  $C_T^2$ , to heights within the range encompassed by the UAS. For the considered case, the average temperature and relative humidity values were  $13^\circ\text{C}$  and  $35\%$ , which results in attenuation due to atmospheric absorption of approximately  $0.016 \text{ dB m}^{-1}$  for the sodar frequency of  $1,900 \text{ Hz}$ .

The speed of sound,  $c$ , is calculated based upon the UAS temperature and humidity measurements according to

$$c = \sqrt{\gamma_a R_d T_{av}}, \quad (15)$$

where  $\gamma_a$  is the specific heat ratio of air,  $R_d$  is the gas constant for dry air ( $287 \text{ J K}^{-1} \text{ kg}^{-1}$ ),  $T_{av}$  is the acoustic virtual temperature in K, and  $c$  is in  $\text{m s}^{-1}$  (Kaimal and Businger 1963).  $T_{av}$  can be calculated from the temperature  $T$  and specific humidity  $q$  as  $T_{av} = T(1 + 0.513q)$ . The value of the backscattering coefficient  $\sigma_s$  can then be estimated using (12), while the sodar-estimated  $C_T^2$  can then be evaluated through Eq. 13.

## 5 Example Case

### 5.1 Experiment Description

On April 24 2013, a field experiment was conducted at the KAEFS site. The UAS performed several flights using a flight plan of repeating circles at prescribed heights, as illustrated in Fig. 1. A Metek PCS.2000 sodar located approximately 150 m from the centre of the UAS flight path was in operation for the duration of the UAS flights. Three flights were performed, and here we use data recorded during the second flight, which took place from 1824 to 1855 local time (LT; 2324–2355 UTC). The experiment time window covers the start of the early evening transition regime, in which the turbulence in the boundary layer begins to decay. Further details about the SMARTSonde, the flights performed during this experiment, and the calculation of  $C_T^2$  from the UAS data can be found in Bonin et al. (2015).

A large-eddy simulation was performed for the time period 1700–1900 LT on April 24, corresponding to the time of the UAS flights. The University of Oklahoma LES (OU-LES, [Fedorovich et al. 2004a](#)) was used in the experiment. The OU-LES code has been tested extensively for convective boundary layer (CBL) conditions, and it has been proven to realistically reproduce mean flow and turbulence structure under clear CBL conditions such as observed during the experiment ([Fedorovich et al. 2001, 2004b](#); [Gibbs et al. 2011](#)).

The simulation was performed using a variable timestep (based upon numerical stability), with an average timestep during the second hour of simulation being 0.4 s. The effective temporal resolution of the OU-LES is  $5-7\Delta t$ , which gives an effective time constant of the LES of about 2.5 s. The domain size was  $X \times Y \times Z = 640 \text{ m} \times 640 \text{ m} \times 3 \text{ km}$ , with a uniform grid spacing of  $\Delta x = \Delta y = \Delta z = 5 \text{ m}$ . The lowest numerical grid level was located at 2.5 m above the ground. The employed subgrid turbulence closure scheme is based upon [Deardorff \(1980\)](#). The LES was nudged with output from a Weather Research and Forecasting (WRF, [Skamarock et al. 2008](#)) model run with a 4-km horizontal grid spacing, centered over the KAEFS site. The WRF model was initialized using data from the North American Regional Reanalysis (NARR, [Mesinger et al. 2006](#)) fields. Horizontal mean profiles of the zonal and meridional winds  $u$  and  $v$ , the specific humidity  $q$ , and the potential temperature  $\theta$  were taken from the WRF output every minute. These profiles were temporally interpolated and used to nudge the corresponding prognostic LES fields at every timestep, as explained in [Gibbs et al. \(2011\)](#).

The mean profiles of potential temperature from the LES and UAS and the horizontal wind components from the LES, UAS, and sodar are illustrated in Fig. 4. The LES is seen to produce slightly warmer atmospheric conditions than sensed by the UAS, although the potential temperature variation with height is very similar in the LES data and UAS measurements. The wind profiles are also seen to be broadly similar, with slightly higher wind speeds measured by the UAS than predicted by the LES at low heights. The mean wind profiles from the sodar are also presented, but the large variation between averaging periods encompassing the flight period indicate that the sodar wind data may be unreliable. For further discussion of the atmospheric conditions during the field experiment see [Bonin et al. \(2015\)](#), who also

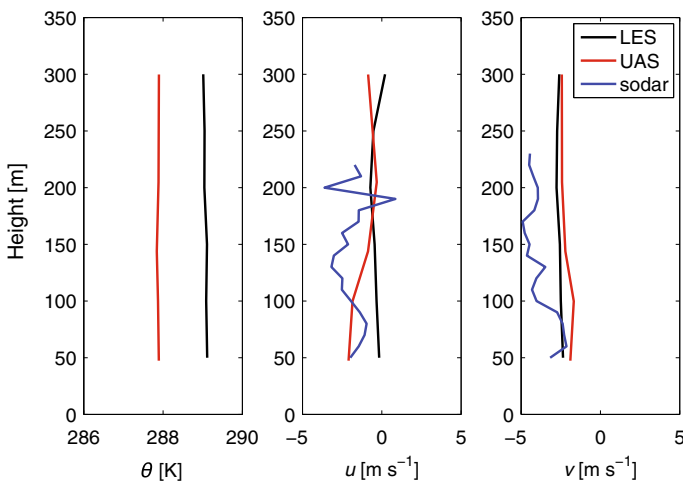


**Fig. 4** Comparison of the mean profiles of potential temperature ( $\theta$ , left panel), zonal wind speed ( $u$ , centre panel) and meridional wind speed ( $v$ , right panel) from the LES, UAS, and sodar

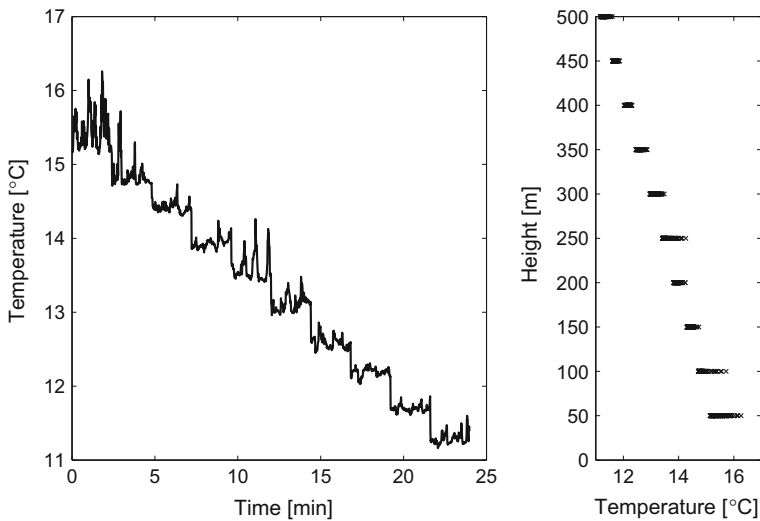


**Fig. 5** *Left panel* a time series of the simulated UAS temperature measurements. *Right panel* the variation of the simulated temperature measurements at each studied height

compare wind speed data from a lidar located at the experimental site, which matches that from the LES more closely than the sodar data.

The UAS simulator was populated with turbulent flow fields from the described LES for the time period 1825–1850 LT, encompassing the duration of the ascending portion of the UAS flight. The simulated flight plan included circles of radius 200 m, at 50-m height increments from 50 to 500 m above the ground (as illustrated in Fig. 1). Two successive circles were simulated at each separate height, with 48 data points collected equidistantly around each circle. The relative ground speed of the simulated UAS for this experiment is approximately  $18 \text{ m s}^{-1}$ . Unlike the real UAS, there was no time delay since the simulated UAS moved from one height up to the next. The ground-relative speed of the simulated UAS also remained unaffected by external factors such as wind speed. Temperature time series from the simulated UAS are illustrated in Fig. 5, where the temperature decrease with height is clearly seen. Figure 5 also shows the relative temperature variation at each height, where the left panel of the figure indicates larger temperature variations during the first few minutes (i.e., at the lowest measurement height) than during the later portion of the flight.

The method outlined in Sect. 4.2 was used to calculate  $C_T^2$  from the simulated UAS temperature data. A similar method (outlined in Sect. 4.3) was also used on the recorded temperature data from the actual UAS flight. The structure-function parameter values derived from the UAS simulator were then compared with their counterparts derived directly from the LES temperature field, while the  $C_T^2$  values derived from the UAS flight were compared with those derived from the sodar data.

## 5.2 Results

It is known that the concept of  $C_T^2$  applies only to locally isotropic turbulence within the inertial subrange of spatial scales. To examine the isotropy of the turbulence over horizontal planes, we compare the four sets of  $(\delta T^2)$  values:  $(\delta T^2)_{|x}$ ,  $(\delta T^2)_{|y}$ ,  $(\delta T^2)_{|xy}$ , and  $(\delta T^2)_{|yx}$ .

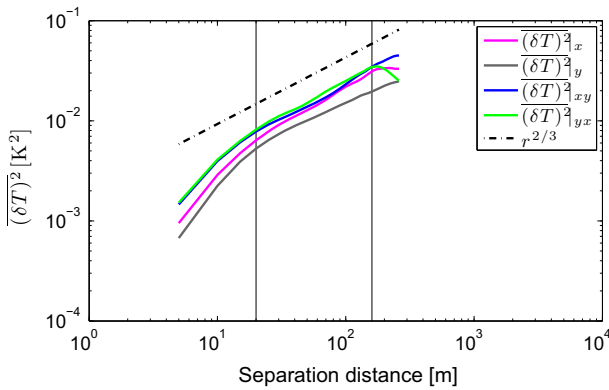


**Fig. 6** Variation of  $\overline{(\delta T^2)}$  with separation distance at a height of 200m from the four direction evaluated directly from LES output. The *black lines* mark the bounds between which the turbulence from the LES is within the inertial subrange

Figure 6 shows the variation of  $\overline{(\delta T^2)}$  along different directions with separation distance, for a height above the ground of 200m. Examining Fig. 6, it can be seen that there is good agreement between  $\overline{(\delta T^2)}_{|x}$ ,  $\overline{(\delta T^2)}_{|xy}$ , and  $\overline{(\delta T^2)}_{|yx}$ , whilst  $\overline{(\delta T^2)}_{|y}$  shows slightly smaller  $C_T^2$  values than the other three directions, most notably at larger separation distances. An investigation into the discrepancy between  $\overline{(\delta T^2)}_{|y}$  and  $\overline{(\delta T^2)}$  evaluated in the other three directions suggested that wind shear is likely responsible for this effect. The simulation contained non-zero wind shear, with a mean value of  $v$  across the domain at a height of 200m being  $-2.7 \text{ m s}^{-1}$  and a corresponding value of  $u$  of  $-0.5 \text{ m s}^{-1}$ . Wind shear acts to elongate turbulent eddies in the dominant wind direction, which reduces temperature differences in this direction (that is, reducing  $\overline{(\delta T^2)}_{|y}$  in this case study). The role of a sheared environment in introducing turbulence anisotropy has been demonstrated for velocity spectra in Gibbs and Fedorovich (2014).

To further examine whether the simulated turbulence is within the inertial subrange of scales, the inertial subrange  $r^{2/3}$  separation distance dependence, Eq. 2, is evaluated. The black dashed line in Fig. 6 represents the  $r^{2/3}$  dependence. Comparing this line to the four  $\overline{(\delta T^2)}$  dependencies one may notice that for separation distances between approximately 20 and 160m, marked by the vertical lines in Fig. 6,  $\overline{(\delta T^2)}$  does indeed follow the  $r^{2/3}$  law when evaluated in the  $x$ ,  $xy$ , and  $yx$  directions. The  $\overline{(\delta T^2)}_{|y}$  values do not follow the  $r^{2/3}$  law quite as closely as the others, apparently due to the influence of wind shear. However, even  $\overline{(\delta T^2)}_{|y}$  scales as approximately  $r^{2/3}$ , indicating that the turbulence can be considered to be approximately within the inertial subrange in the separation distance range marked by the black lines in Fig. 6 (20–160m).

The slight anisotropy of the turbulence introduces the question of whether the calculation of  $C_T^2$  is appropriate. However, it would be natural to expect that wind shear of some magnitude will be present (possibly causing anisotropy of the turbulence) in most field experiments designed to investigate  $C_T^2$ . Thus, it was decided that within the range  $20 \text{ m} \leq r \leq 160 \text{ m}$ , the evaluation of the  $C_T^2$  from the simulated flow data is justified. It must be noted that since only a subset of the entire LES domain was utilized for these experiments, there are obviously a greater number of available temperature differences at smaller separation distances, and few temperature differences at the largest separations. The relatively fewer numbers of

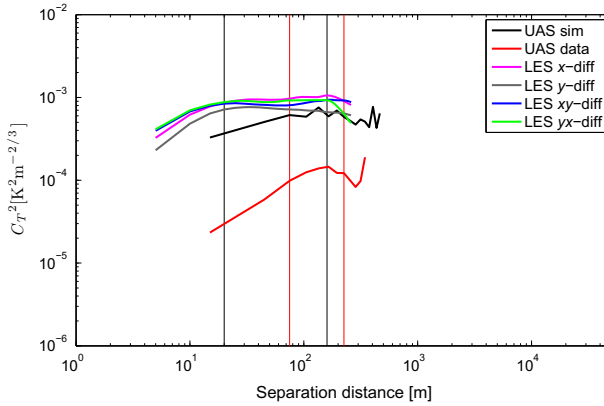


**Fig. 7** Variation of  $C_T^2$  with separation distance at a height of 200 m a.g.l. The *black lines* mark the bounds between which the turbulence from the LES is within the inertial subrange, and the *red lines* show the inertial subrange identified from the UAS measurements

temperature pairs contributing to the  $\overline{(\delta T^2)}$  (and thus  $C_T^2$ ) at the largest values of  $r$  suggests lower confidence in these values than those for small  $r$ .

The  $C_T^2$  values were calculated from both the LES flow fields directly and from the output of the UAS simulator. Corresponding  $C_T^2$  values were also calculated from the actual UAS and sodar data recorded during the KAEFS field experiment. The presence of the inertial subrange in the UAS turbulence data is examined by comparing  $C_T^2$  at a range of separation distances. For separation distances to be considered within the inertial subrange,  $C_T^2$  values should be approximately constant with separation distance (assuming that  $\overline{(\delta T^2)} \propto r^{2/3}$ ). The  $C_T^2$  values derived from the UAS flight data (red line in Fig. 7) show considerable variation within the inertial subrange identified from the LES  $C_T^2$  data (black vertical lines in Fig. 7), as do the  $C_T^2$  values calculated from the UAS simulator. The inertial subrange that could be seen in the UAS  $C_T^2$  measurements was also identified and is marked on Fig. 7 by the vertical red lines. Within the UAS-derived inertial subrange, the  $C_T^2$  measurements vary by no more than 12%. The bounds of the inertial subrange identified from these two measurement sets clearly differ, with the LES data showing the lower bound of the inertial subrange at a considerably lower value (20 m) than the UAS data (75 m). One reason for this discrepancy is the 3-s time constant of the UAS temperature sensor. Since the UAS is travelling at an airspeed of  $15 \text{ m s}^{-1}$ , this results in unreliable estimates of  $C_T^2$  below separation distances of 45 m. This is clearly a limitation of the particular temperature sensor used on the UAS; the effect of the temperature sensor time constant is discussed further below. Although sodar returns result from Bragg scattering related to a particular separation distance, we do not assign a separation distance value, and so the sodar-derived  $C_T^2$  data are examined as vertical profiles only. Assigning a separation distance to the  $C_T^2$  data derived from the sodar would result in an unfair comparison, since the other methods used in this study evaluate  $C_T^2$  over horizontal planes only, while the sodar-derived  $C_T^2$  also contains contributions from vertical temperature differences. It is clearly seen in Fig. 7 that the values of  $C_T^2$  calculated from the recorded UAS data are approximately an order of magnitude smaller than the values calculated from the simulated UAS and directly from the LES data. Two potential reasons for this disparity are outlined below.

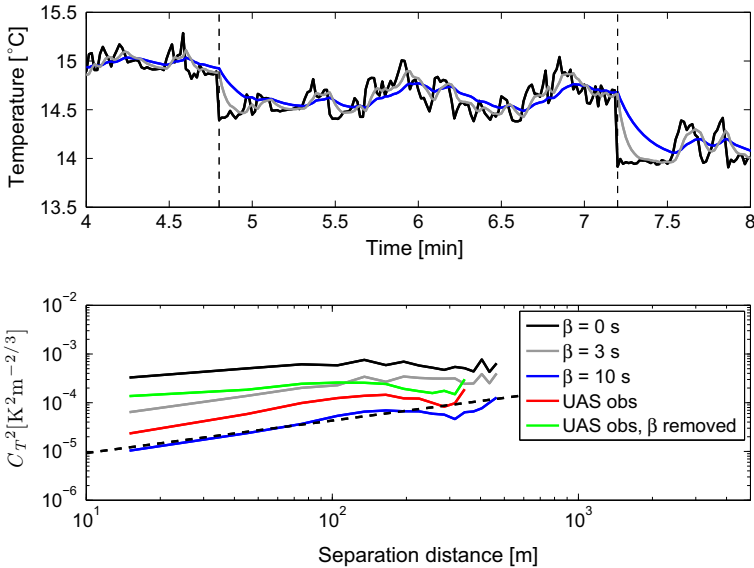


**Fig. 8** Upper panel the simulated temperature measurements at 200-m height with time constants of  $\beta=0$  (black),  $\beta=3$  s (blue), and  $\beta=10$  s (grey). The vertical dashed lines mark the time the simulated UAS was at 200-m height. Lower panel the resulting  $C_T^2$  values from the temperature data in the upper panel. The red line shows  $C_T^2$  from the observed UAS data, and the green line shows  $C_T^2$  calculated from the UAS data when the time constant has been corrected for. The slope of the black dashed line shows the relationship between  $C_T^2$  and separation distance that results from a horizontally isothermal atmosphere

The first possible reason is associated with the time constant of the UAS temperature sensor. The time constant of the temperature probe represents the time it takes the sensor to fully respond to a new temperature value. The UAS temperature sensor was experimentally calibrated, finding a time constant of 3 s for an airspeed of  $15 \text{ m s}^{-1}$  (corresponding to the airspeed used by the UAS during the flights on April 24). The  $C_T^2$  values calculated using the UAS simulator do not include the effects of the time constant on the simulated temperature measurements. To examine this effect, a second experiment was performed using the UAS simulator, in which a time constant was included. The effect of the time constant was included in the simulated temperature measurements as

$$T_{\beta}(t + 1) = T_{\beta}(t) + (1 - \exp(-\Delta t/\beta)) [T(t + 1) - T_{\beta}(t)], \tag{16}$$

where  $T_{\beta}(t)$  represents the temperature with the inclusion of the time constant at time  $t$ ,  $\Delta t$  is the timestep used in the UAS simulator,  $\beta$  is the time constant, and  $T(t)$  is the original temperature measurement at time  $t$  (without the time constant included). Two values for the time constant were tested,  $\beta=3$  s, and an increased value of  $\beta=10$  s. These  $\beta$  values were chosen since experimental calibration of the UAS temperature sensor found that a time constant of 3 s is applicable for an airspeed of  $15 \text{ m s}^{-1}$ , which was the airspeed of the UAS during the measurements, and the 10-s  $\beta$  value is used to illustrate the effect of the time constant at low airspeeds. The airspeed of the simulated UAS was  $18 \text{ m s}^{-1}$ , for which a time constant of 2.8 s is applicable (determined through experimental calibration of the sensor).

The effect of the inclusion of the time constant is illustrated in Fig. 8. The upper panel shows the temperature measurements obtained at a height of 200 m for the cases with no

time constant included (black line) and with time constants of 3 s (grey line) and 10 s (blue line). It is clear that the addition of the time constant acts to smooth the temperature data, and this smoothing is most noticeable when the UAS moves from one height to the next (marked in the upper panel of Fig. 8 by the dashed lines). It follows that reducing the temperature variability in this manner will result in lower values of  $C_T^2$ . This reduction is demonstrated in the lower panel of Fig. 8, which shows the  $C_T^2$  values resulting from the temperature data in the upper panel. The  $C_T^2$  values decrease considerably when a time constant is introduced, and the magnitude of this reduction increases for a larger time constant. Such an effect may be expected, since the addition of the time constant acts to reduce variability in the temperature data. As can be seen in the lower panel of Fig. 8, the addition of the time constant has the greatest effect on  $C_T^2$  values at the smallest separation distances with less effect at larger separation distances. It should be noted that during the calculation of  $C_T^2$  from temperature data including a time constant, the first  $\beta + 1$  points were excluded from the temperature time series at each height in order to remove contamination of the data by temperatures from the previous height. The inclusion of  $\beta$  in the temperature data also affects the constancy of  $C_T^2$  with separation distance, due to the smoothing of the temperature data. With an increased value of  $\beta$ , the temperature variability tends to zero. For such a constant temperature field,  $(\delta T^2)$  is zero across all separation distances. Thus, the increase of the time constant translates to a  $r^{2/3}$  variation of  $C_T^2$  with separation distance. The dashed line in the lower panel of Fig. 8 illustrates this relationship, and it is seen that the addition of the time constant brings the  $C_T^2$  variation with separation distance closer to the relation for isothermal conditions.

The measured temperature time series from the UAS was also revised to attempt to mitigate the effect of the 3-s time constant. To do this, we applied a simple first-order correction using Eq. 16 rearranged as

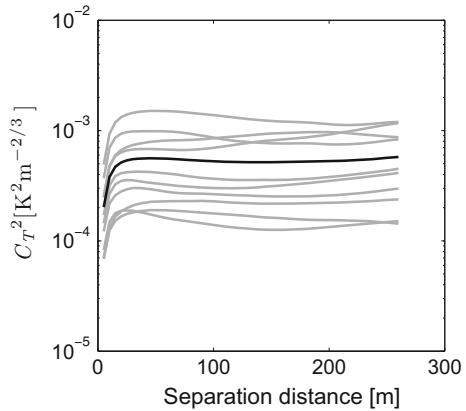
$$T(t + 1) = \frac{T_\beta(t + 1) - T_\beta(t)}{(1 - \exp(-\Delta t/\beta))} + T_\beta(t). \quad (17)$$

The effect of applying this correction factor on the resulting  $C_T^2$  is shown by the green line in the lower panel of Fig. 8, where the original  $C_T^2$  values from the UAS data (without the correction factor applied) are shown in red. All of the data displayed in the lower panel of Fig. 8 account for advection correction. It is seen that removing the effect of the time constant (albeit using a rather crude method) does act to increase  $C_T^2$  retrieved from the UAS measurements, most notably at smaller separation distances. We note that this correction factor should only be applied if the time constant of the temperature sensor is known and calibrated for the airspeed of the UAS.

While it is seen in Fig. 8 that the inclusion of the time constant decreases  $C_T^2$ , bringing the simulated  $C_T^2$  values closer in line with the UAS observations, the observed  $C_T^2$  values do not demonstrate the same separation-distance dependence as the simulated  $C_T^2$  values with non-zero  $\beta$ . When the effect of the time constant is removed from the UAS temperature data, the  $C_T^2$  values are increased, bringing them closer in line with those from the UAS simulator. The separation distance dependence of  $C_T^2$  also changes when the UAS data are corrected for the time constant, coming closer to the flat line expected from the  $r^{2/3}$  law in the lower panel of Fig. 8. This suggests that a broader portion of the true inertial subrange could be captured if the UAS data are corrected to account for the time constant. However, further study would be needed, as the correction applied here is a simple first-order equation that does not replace the full temperature variability removed by the effect of the time constant.

A second possible reason for the reduced observed  $C_T^2$  values compared to the values calculated from the LES is that local effects (i.e., site-specific characteristics such as small-

**Fig. 9** Dependence of  $C_T^2$  on separation distance for the LES data at a height of 200 m. The grey lines represent 2.4-min temporal averages taken from 24 min of LES output, while the black line represents an average of the full 24 min of data used in the UAS simulator



scale topographical effects, flow blockage by vegetation, spatially-varying roughness lengths caused by differing land surfaces and vegetation) are not adequately captured by the relatively coarse nudging data provided by the WRF model. This may result in the LES and UAS data not representing exactly the same meteorological situation.

Another limitation of using the UAS to measure  $C_T^2$  is associated with the time period over which measured  $C_T^2$  values are representative of the atmospheric conditions. The availability of the LES data enables an examination of the variation of  $C_T^2$  over different time periods during the simulation. Figure 9 illustrates this variation, showing values of  $C_T^2$  calculated from LES data over the course of the 24-min period used to populate the UAS simulator. The grey lines represent spatial averages across the domain, at a height of 200 m, with a 2.4-min averaging time, which is the time period during which the simulated UAS remains at a single height. The black line represents  $C_T^2$  values obtained over the 24-min period, which is equal to the duration of the simulated UAS flight.

It is clear from Fig. 9 that the 24-min  $C_T^2$  values provide a good measure of the thermal variability over the range of scales examined by the simulated UAS, i.e., for  $r=25\text{--}250$  m. However, the 24-min  $C_T^2$  values cannot capture the variation of the temperature within the representative range of its boundary-layer variability. It is also seen in Fig. 9 that the 2.4-min values of  $C_T^2$  vary within an order of magnitude during the 24-min period. The high spatial and temporal variations of  $C_T^2$ , especially in the convective boundary layer, are a well-known feature that has been examined in detail for  $C_T^2$  derived from LES of the CBL by [Cheinet and Siebesma \(2009\)](#).

The wide range of measured  $C_T^2$  values over that 24-min period also suggests that slight discrepancies between the  $C_T^2$  values from the UAS simulator and directly from the LES data should be expected. The UAS simulator provides a  $C_T^2$  measurement at each height that represents an average taken over 2.4 min, while the values derived from the LES directly represent a 24-min time interval.

Aside from examining the variation of  $C_T^2$  with separation distance, use of the flight plan in Fig. 1 allows for an examination of the variation of  $C_T^2$  with height. The vertical profiles of  $C_T^2$  at 50-m separation distance, both from the LES data sampled in different directions and the UAS simulator, are, again, similar in magnitude (Fig. 10, left panel). Minor differences among the profiles are primarily due to the different averaging times used by each method, and due to the smaller areal coverage of the UAS simulator. The simulated UAS spends 2.4 min at each height of interest, while in the direct  $C_T^2$  evaluation from LES an averaging time

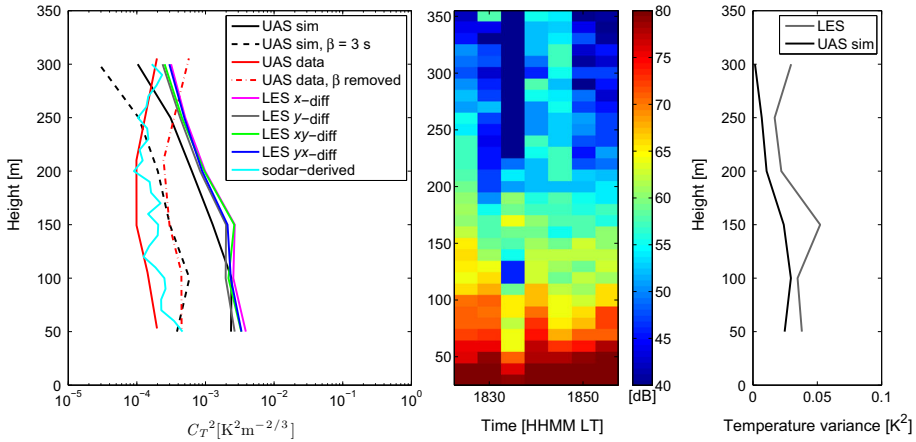


**Fig. 10** Left panel the variation of  $C_T^2$  with height via all the examined calculation methods. The separation distance used in the both the LES and UAS-based calculations is 50 m. Centre panel sodar power return for the duration of the UAS flight. Right panel profiles of temperature variance across the whole LES domain (grey) and across the subset samples by the UAS simulator (black)

of 24 min for each height is used. For  $C_T^2$  derived from UAS data, the entire profile shows smaller  $C_T^2$  values compared to the values provided by the other methods. Even when the same averaging time is used at each height (i.e., when the LES data are averaged across the domain only for the duration of the simulated UAS flight at that height), there are still differences in the temperature variability due to sampling a greater number of spatial points in the direct LES  $C_T^2$  evaluation than in the UAS simulator. This feature is illustrated in the right panel of Fig. 10, which shows the temperature variance calculated from the UAS simulator data (black line) and the LES (grey line) over the 2.4-min periods of the simulated UAS remaining at each height. It can be seen that only sampling a subset of the LES domain at each height (i.e., the circular flight path rather than the whole plane) creates a reduction in the measured temperature variance. Differences are also seen between the simulated measurements from the LES and UAS simulator and those from the UAS data. As discussed previously, two possible causes for this are the time inertia of the temperature sensor, and possible disparity between meteorological conditions reproduced by the LES and captured by the UAS observations. The profile generated by correcting the measured UAS data for the time constant is shown by the red dashed line, and the time constant removal is again seen to increase the value of the measured  $C_T^2$ , although it does not alter the shape of the profile (since the same time constant removal is applied at each height).

The sodar model used for this experiment provides returned power in units of dB, with an arbitrarily set zero value (illustrated for the case in this study in the right panel of Fig. 10). Typical values of returned power are between 40–80 dB. Directly using these values results in unphysically high  $C_T^2$  values, so a multiplicative constant is applied to bring  $C_T^2$  down to a reasonable level. The same constant is used for all times and heights, so that  $C_T^2$  profiles remain self-consistent. This implies that comparisons in vertical variations of  $C_T^2$  from the different instruments are meaningful, but evaluation of  $C_T^2$  using the sodar method should be performed with this consideration in mind. The noted correction does not affect any of the other methods used in this study, which employ directly measured (or modelled) temperature values to calculate  $C_T^2$ . For this reason, we suggest that  $C_T^2$  values derived from uncalibrated sodars should be used either for monitoring temporal changes in  $C_T^2$  at a certain

height, or for comparing vertical profiles of  $C_T^2$  over time. The  $C_T^2$  profiles derived from UAS and sodar data (the red and cyan lines, respectively, in Fig. 10) agree very well. Greater confidence is placed in the  $C_T^2$  values in the lower portion of the sodar-derived profiles, as the sodar returned power decreases sharply with height, as seen in the right panel of Fig. 10. In contrast, equal confidence is placed in the UAS data across the height range examined. The good agreement across the height range examined by the UAS and sodar (50–300 m), both of which use data from the field experiment, provides a measure of confidence in each method.

## 6 Conclusions

One of the goals of the reported study was to test how accurately a UAS platform can determine the structure-function parameter of turbulent temperature fluctuations,  $C_T^2$ . This capability was investigated through the use of a UAS simulator, which incorporates numerical LES data to reproduce temperature measurements from the UAS. The same processing techniques were implemented on the simulated UAS data to calculate  $C_T^2$  as are used on the actual UAS temperature measurements.

A major caveat in the method utilized is that when comparing  $C_T^2$  profiles and separation-distance dependence between the measured and simulated UAS, a direct comparison cannot be easily carried out. Discrepancies between the atmospheric state during the field experiment and the state reproduced by the LES appear to cause differences between the  $C_T^2$  values derived from the real and simulated UAS measurements. It is also shown that the addition of an appropriate time constant to the UAS simulator reduced the discrepancy between the measured and simulated UAS  $C_T^2$  values. The time constant acts to reduce  $C_T^2$  values, due to its temporal smoothing effect upon measured temperature, and should be accounted for when using UAS observations for examining  $C_T^2$ . A simple method for removing the effects of the time constant in the UAS data is described, but this method relies on accurate knowledge of the time constant for the airspeed at which the UAS flight is conducted, and it may not accurately account for the full temperature variability that is lost through inertia of the temperature sensor.

Comparisons between  $C_T^2$  from the UAS simulator and LES show good agreement in both height and separation distance (Figs. 7, 10). This indicates that the method used to calculate  $C_T^2$  from UAS data in this study can provide results that are realistic and representative of the atmospheric state reproduced by LES. Once the technique was validated using the UAS simulator, it was tested on temperature measurements from a UAS during a field experiment in central Oklahoma. Height profiles of  $C_T^2$  values derived from the UAS data compare well in shape to those derived from a co-located sodar. Further details of the field experiment, and an in-depth observational analysis of the UAS  $C_T^2$  data are presented in [Bonin et al. \(2015\)](#).

We suggest that while UAS temperature and location data can generally be used to estimate  $C_T^2$ , these data should be employed keeping the following caveats in mind. It must be recognized that the time spent at each height by the UAS is relatively short, particularly for the purpose of the statistically representative characterization of turbulence under convective conditions, and that derived  $C_T^2$  values are representative only for the time period at each height. Given the wide variation of  $C_T^2$  within a 24-min period shown in Fig. 9, it should be kept in mind that  $C_T^2$  values derived from UAS measurements are probably not generally representative of characteristic temperature-variation scales at the measurement height. The time constant of the temperature sensor should also be accounted for, as its inclusion can have a large impact on the derived  $C_T^2$  values, as is demonstrated in Fig. 8. Accounting for the

advection of turbulence past the UAS is also important, particularly for cases during which wind speeds are high. For this study, such advection was taken into account in the calculation of the separation distance. For a more complete discussion on the effect of advection of turbulence upon  $C_T^2$  values computed using UAS data, see Bonin et al. (2015). With the aforementioned considerations kept in mind, UAS offers a promising platform for providing *in-situ* measurements of  $C_T^2$  in the boundary layer over short time periods.

**Acknowledgments** The National Science Foundation (NSF) is acknowledged for the support of the reported study through the Grant ATM-1016153. The authors acknowledge the three anonymous reviewers whose suggestions substantially improved the manuscript.

## References

- Asimakopoulos DN, Cole RS, Caughey SJ, Crease BA (1976) A quantitative comparison between acoustic sounder returns and the direct measurement of atmospheric temperature fluctuations. *Boundary-Layer Meteorol* 19:137–147
- Balsley BB (2008) The cires tethered lifting system: a survey of the system, past results, and future capabilities. *Acta Geophys* 56(1):21–57
- Bonin TA, Chilson PB, Zielke B, Fedorovich E (2012) Observations of early evening boundary layer transitions using a small unmanned aerial system. *Boundary-Layer Meteorol* 2:1–14. doi:10.1007/s10546-012-9760-3
- Bonin TA, Chilson PB, Zielke BS, Klein PM, Leeman JR (2013) Comparison and application of wind retrieval algorithms for small unmanned aerial systems. *Geosci Instrum Method Data Syst* 2:177–187
- Bonin TA, Goines D, Scott A, Wainwright CE, Gibbs JA, Chilson PB (2015) Measuring structure function parameters with a small unmanned aerial system. *Boundary-Layer Meteorol*, (in press)
- Cheinet S, Cumin P (2011) Local structure parameters of temperature and humidity in the entrainment-drying convective boundary layer: a large-eddy simulation analysis. *J Appl Meteorol Climatol* 50(2):472–481
- Cheinet S, Siebesma AP (2009) Variability of local structure parameters in the convective boundary layer. *J Atmos Sci* 66(4):1002–1017
- Deardorff JW (1980) Stratocumulus-capped mixed layer derived from a three-dimensional model. *Boundary-Layer Meteorol* 18:495–527
- Fedorovich E, Nieuwstadt FTM, Kaiser R (2001) Numerical and laboratory study of horizontally evolving convective boundary layer. Part I: transition regimes and development of the mixed layer. *J Atmos Sci* 58:70–86
- Fedorovich E, Conzemius R, Esau I, Chow FK, Lewellen D, Moeng CH, Pino D, Sullivan P, de Arellano JVG (2004a) Entrainment into sheared convective boundary layers as predicted by different large eddy simulation codes. In: Preprints, 16th Symposium on boundary layers and turbulence. American Meteorological Society, 9–13 August, Portland, Maine, USA, pp CD-ROM, P4.7
- Fedorovich E, Conzemius R, Mironov D (2004b) Convective entrainment into a shear-free, linearly stratified atmosphere: bulk models reevaluated through large eddy simulations. *J Atmos Sci* 61:281–295
- Frehlich R (1992) Laser scintillation measurements of the temperature spectrum in the atmospheric surface layer. *J Atmos Sci* 49(16):1494–1509
- Gibbs J, Fedorovich E (2014) Comparison of convective boundary layer velocity spectra retrieved from large eddy simulation and weather research and forecasting model data. *J Appl Meteorol Climatol* 53(2):377–394
- Gibbs JA, Fedorovich E, van Eijk AMJ (2011) Evaluating weather research and forecasting (WRF) model predictions of turbulent flow parameters in a dry convective boundary layer. *J Appl Meteorol Climatol* 50(12):2429–2444
- Gur'yanov AE, Kallistratova MA, Martvel FE, Pequr MS, Petenko IV, Time NS (1987) Comparison of sodar and microfluctuation measurements of the temperature structure parameter in mountainous terrain. *Atmos Ocean Phys* 23(9):685–691
- Gur'yanov AE, Kallistratova MA, Kuttyrev AS, Petenko IV, Shcheglov PV, Tokovinin AA (1992) The contribution of the lower atmospheric layers to the seeing at some mountain observatories. *Astron Astrophys* 262:373–381
- Holland GJ, adn JA, Curry PJW, Tyrell G, Gauntlett D, Brett G, Becker J, Hoag R, Vaglianti W (2001) The aerosonde robotic aircraft: a new paradigm for environmental observations. *Bull Am Meteorol Soc* 82:889–901

- ISO9613-1 S Geneva (1993) Acoustics—attenuation of sound during propagation outdoors—part 1: calculation of the absorption of sound by the atmosphere. ISO9613-1:1993(E)
- Kaimal JC, Businger JA (1963) A continuous wave sonic anemometer-thermometer. *J Appl Meteorol* 2:156–164
- Kumar MS, Anandan VK, Kesarkar A, Narasimha PN (2011) Doppler sodar observations of the temperature structure parameter during moonsoon season over a tropical rural station, Gadanki. *J Earth Syst Sci* 120(1):65–72
- Kunkel KE, Walters DL, Ely GA (1981) Behavior of the temperature structure parameter in a desert basin. *J Appl Meteorol* 20(2):130–136
- Little CG (1969) Acoustic methods for the remote probing of the lower atmosphere. *Proc IEEE* 57:571–578
- Maronga B, Moene AF, van Dinter D, Raasch S, Bosveld FC, Gioli B (2013) Derivation of structure parameters of temperature and humidity in the convective boundary layer from large eddy simulations and implications for the interpretation of scintillometer observations. *Boundary-Layer Meteorol* 148(1):1–30
- Mesinger F, DiMego G, Kalnay E, Mitchell K, Shafran PC, Ebisuzaki W, Woollen J, Jović D, Rogers E, Berbery EH, Ek MB, Fan Y, Grumbine R, Higgins W, Li H, Lin Y, Manikin G, Parrish D, Shi W (2006) North American regional reanalysis. *Bull Am Meteorol Soc* 87(3):343–360
- Muschinski A, Sullivan PP, Wuertz DB, Hill RJ, Cohn SA, Lenschow DH, Doviak RJ (1999) First synthesis of wind-profiler signals on the basis of large-eddy simulation data. *Radio Sci* 34(6):1437–1459
- Neff WD (1975) Quantitative evaluation of acoustic echoes from the planetary boundary layer. *J Atmos Sci* 36:1820–1821
- Peltier LJ, Wyngaard JC (1995) Structure-function parameters in the convective boundary layer from large-eddy simulation. *J Atmos Sci* 52(21):3641–3660
- Petenko I, Argentini S, Pietroni S, Viola A, Mastrantonio G, Casasanta G, Arisitidi E, Bouchez G, Agabi A, Bondoux E (2014a) Observations of optically active turbulence in the planetary boundary layer by sodar at the Concordia astronomical observatory, Dome C. Antarctica. *Astron Astrophys* 568:A44
- Petenko I, Mastrantonio G, Viola A, Argentini S, Pietroni I (2014b) Some statistics of the temperature structure parameter in the convective boundary layer observed by sodar. *Boundary-Layer Meteorol* 150(2):215–233
- Readings CJ, Butler HE (1972) The measurement of atmospheric turbulence from a captive balloon. *Meteorol Mag* 101:286–298
- Scipión DE, Chilson PB, Fedorovich E, Palmer RD (2008) Evaluation of an LES-based wind profiler simulator for observations of a daytime atmospheric convective boundary layer. *J Atmos Ocean Technol* 25:1423–1436
- Shuqing M, Hongbin C, Gai W, Yi P, Qiang L (2004) A miniature robotic plane meteorological sounding system. *Adv Atmos Sci* 21(6):890–896
- Skamarock WC, Klemp JB, Dudhia J, Gill DO, Barker DM, Wang W, Powers JG (2008) A description of the advanced research WRF version 3. Tech. Rep, NCAR, USA
- Spieß T, Bange J, Buschmann M, Vörsmann P (2007) First application of the meteorological Mini-UAV ‘M2AV’. *Meteorol Z* 16:159–169
- Tatarskii VI (1961) Wave propagation in a turbulent medium. McGraw-Hill, New York 285 pp
- Tatarskii VI (1971) The effects of the turbulent atmosphere on wave propagation. Kefer Press, Jerusalem 472 pp
- Taylor GI (1938) The spectrum of turbulence. *Proc R Soc Ser A* 164:476–490
- Thomson D, Coulter R, Warhaft Z (1978) Simultaneous measurements of turbulence in the lower atmosphere using sodar and aircraft. *J Appl Meteorol* 17:723–734
- Travouillon T, Ashley MCB, Burton MG, Storey JWV, Loewenstein RF (2003) Atmospheric turbulence at the South Pole and its implications for astronomy. *Astron Astrophys* 400:1163–1172
- Tunick A (2005) Toward increasing the accuracy and realism of future optical turbulence calculations. *Meteorol Atmos Phys* 90:159–164
- van den Kroonenberg A, Martin T, Buschmann M, Bange J, Vörsmann P (2008) Measuring the wind vector using the Autonomous Mini Aerial Vehicle M2AV. *J Atmos Ocean Technol* 25:1969–1982
- van den Kroonenberg AC, Martin S, Beyrich F, Bange J (2012) Spatially-averaged temperature structure parameter over a heterogeneous surface measured by an Unmanned Aerial Vehicle. *Boundary-Layer Meteorol* 142:55–77
- Weill A, Klapisz C, Strauss B, Baudin F, Jaupart C, Grunderbeeck PV, Goutorbe JP (1980) Measuring heat flux and structure functions of temperature fluctuations with an acoustic doppler sodar. *J Appl Meteorol* 19:199–205
- Wilson C, Fedorovich E (2012) Direct evaluation of refractive-index structure functions from large-eddy simulation output for atmospheric convective boundary layers. *Acta Geophys* 60(5):1474–1492

- Wood CR, Kouznetsov RD, Gierens R, Nordbo A, Järvi L, Kallistratova MA, Kukkonen J (2013) On the temperature structure parameter and sensible heat flux over Helsinki from sonic anemometry and scintillometry. *J Atmos Oceanic Technol* 30(8):1604–1615
- Wyngaard JC, Izumi YSA, Collins J (1971) Behavior of the refractive-index-structure parameter near the ground. *J Opt Soc Am* 61(12):1646–1650